
Dynamics for the Dynamic Frank Harris: Exploring $\text{H}^+ + \text{CF}_4$ at $E_{\text{Lab}} = 20$ and 30 eV

BUDDHADEV MAITI,¹ PATRICK M. MCLAURIN,¹
RAYMOND SADEGHI,² S. AJITH PERERA,³ JORGE A. MORALES¹

¹*Department of Chemistry and Biochemistry, Texas Tech University, PO Box 41061, Lubbock, TX 79409-1061*

²*Department of Chemistry, University of Texas at San Antonio, One UTSA Circle, San Antonio, TX 78249-0698*

³*Department of Chemistry, Quantum Theory Project, Gainesville, FL 32611*

Received 23 January 2009; accepted 19 February 2009

Published online 30 April 2009 in Wiley InterScience (www.interscience.wiley.com).

DOI 10.1002/qua.22205

ABSTRACT: The $\text{H}^+ + \text{CF}_4$ reaction at collision energies $E_{\text{Lab}} = 20$ and 30 eV is investigated with the electron nuclear dynamics (END) theory. The level of END herein employed prescribes a classical-mechanics description for the nuclei and a single-determinantal representation for the electrons. The results include visualizations of the simulated collisions, and calculations of various scattering properties. The present simulations always predict noncharge-transfer scattering (NCTS) for $\text{H}^+ + \text{CF}_4$ and exclude charge-transfer, dissociation, and rearrangement reactions. The predicted rainbow angles and the total NCTS differential cross sections agree satisfactorily with the available experimental results. The present results are compared with those of the previously simulated $\text{H}^+ + \text{CH}_4$. © 2009 Wiley Periodicals, Inc. *Int J Quantum Chem* 109: 3026–3035, 2009

Key words: electron nuclear dynamics; proton-molecule collisions

Correspondence to: Jorge A. Morales; e-mail: jorge.morales@ttu.edu

Buddhadev Maiti is currently at Department of Chemistry, Penn State University, University Park, PA 16802.

Contract grant sponsor: National Science Foundation.

Contract grant number: CHE-0645374.

Contract grant sponsor: Robert A. Welch Foundation.

Contract grant number: D-1539.

Contract grant sponsor: American Chemical Society Petroleum Research Fund.

1. Introduction

Proton-molecule collision experiments can reveal various microscopic details of chemical reactions [1–10]. Unlike other ionic probes, proton projectiles display an exceptional combination of properties that makes them quite suitable for those studies. For example, proton projectiles possess no molecular structure and therefore cannot experience rovibrational excitations during collisions, but they can provoke and confine those phenomena on their collision partners. Moreover, a proton projectile can capture an electron from a molecular target and thus probe charge-transfer reactions. More significantly, proton-molecule collision experiments are not only relevant for chemical dynamics studies but also for chemical applications. That last aspect is easy to recognize from the astonishing ubiquity of proton-molecule collisions in plasma reactions, particle accelerator processes, combustion and fusion reactions, upper atmosphere phenomena, and astrophysical processes.

Among several proton-scattering experiments reported in the literature, those conducted by the Gentry [1], Linder [2], and Toennies [3–10] groups have provided detailed descriptions of various proton-molecule reactions at collision energies in the $10 \leq E_{\text{Lab}} \leq 46$ eV range. In those studies, time-of-flight analyses of the scattered projectiles (protons in noncharge-transfer reactions and hydrogen atoms in charge-transfer ones) revealed information about the targets' excitations during the collisions. Molecules investigated in that way included: H_2 [1, 3], N_2 [1, 2], O_2 [4], CO [1, 2], NO [2], HF [1, 5], HCl [1], H_2O [6], CO_2 [7], N_2O [7], CH_4 [8], C_2H_2 [9], CF_4 [10], and SF_6 [10] *inter alia*. Although those experiments rendered detailed descriptions of the scrutinized reactions, several microscopic aspects in those processes were not accessible by experimental means. For example, those experiments can not supply a step-by-step record of the reactants transforming into the products and of the electronic charge density evolving in the course of the collision. In principle, that valuable mechanistic information can be obtained via computer simulations of the experiments; therefore, the application of advanced theoretical methods to those processes become necessary if further insight into them is desired. Conversely, the previous experiments can assess the accuracy of a given theoretical method. Then, the successfully tested methods can be used in a predictive fashion to simulate proton-molecule reactions for which there are no experiments. Unfortunately, because of the complexity of some proton-molecule ex-

periments, few of those systems were initially simulated with advanced theoretical methods. Early attempts in that direction included the simulation of a $\text{H}^+ + \text{H}_2$ experiment [3], first with the trajectory surface hopping method [3, 11], and later with the more advanced infinite order sudden approximation method [12]. However, the development of the electron nuclear dynamics (END) [13] theory by Deumens and Öhrn provided a convenient methodology to systematically simulate more complex proton-molecule experiments. END is a time-dependent, direct, nonadiabatic method, and precisely those attributes make END adequate to study proton-molecule reactions. For instance, by being direct, END does not require predetermined potential energy surfaces to run; and by being nonadiabatic, END can describe both the noncharge-transfer and charge-transfer processes in the previous experiments. In fact, previous END simulations of proton-molecule reactions (e.g., $\text{H}^+ + \text{H}_2$ [14], $\text{H}^+ + \text{CH}_4$ [15], $\text{H}^+ + \text{C}_2\text{H}_2$ [16, 17], $\text{H}^+ + \text{H}_2\text{O}$ [18], $\text{H}^+ + (\text{H}_2\text{O})_2$ [19], etc.) have provided good descriptions of those systems and predicted several properties that agreed well with the available experimental data.

In a similar vein, we present herein a preliminary END study of the $\text{H}^+ + \text{CF}_4$ reaction at the collision energies $E_{\text{Lab}} = 20$ and 30 eV. This investigation is the natural continuation of the previous END study of $\text{H}^+ + \text{CH}_4$ at $E_{\text{Lab}} = 30$ eV [15] because it permits comparing the reactivity of two related tetrahedral molecules with different chemical properties. The $\text{H}^+ + \text{CF}_4$ system has been studied experimentally by the Toennies group in two separate investigations [8, 10]. One investigation [8], at the collision energies $E_{\text{Lab}} = 20$ and 30 eV, concentrated on the scattering properties of $\text{H}^+ + \text{CF}_4$ (e.g., differential cross sections, DCS) in comparison with those of $\text{H}^+ + \text{CH}_4$. The other investigation [10], at lower collision energies ($E_{\text{Lab}} = 14.6$ eV and others), concentrated on the CF_4 vibrational excitations during collision. However, unlike $\text{H}^+ + \text{CH}_4$, $\text{H}^+ + \text{CF}_4$ poses a significant challenge for time-dependent, direct-dynamics simulations because of its elevated number of electrons (42 electrons in total). For that reason, this END investigation will only explore some reactive and scattering aspects of the $\text{H}^+ + \text{CF}_4$ experiments at $E_{\text{Lab}} = 20$ and 30 eV [8]. The results of this preliminary investigation are very promising and give an impetus for more exhaustive studies of the present systems and of the remaining experiments [10] in the future.

This investigation of $\text{H}^+ + \text{CF}_4$ at $E_{\text{Lab}} = 20$ and 30 eV is organized as follows. In Section 2, we briefly discuss the END theory as the selected meth-

odology to study the $\text{H}^+ + \text{CF}_4$ reaction; in Section 3, we provide relevant computational details of the present END simulations; in Section 4, we report and discuss the main END results for the $\text{H}^+ + \text{CF}_4$ system in comparison with available experimental data; finally, in Section 5, we present some concluding remarks.

2. Theoretical Background

The END theory has been created by Deumens and Öhrn [20]. In this section, END is succinctly outlined in the context of the present investigation; more detailed discussions on END can be found in Refs. [20, 21]. END is a time-dependent, direct, nonadiabatic method that treats simultaneously the nuclei and electrons of a molecular system. Within that characterization, END admits different levels of realizations according to its description of the nuclear and electronic degrees of freedom [21]. The simplest realization of END prescribes a classical-mechanics description for the nuclei and a single-determinantal representation for the electrons. That simplest END realization is adequate to simulate $\text{H}^+ + \text{CF}_4$ at $E_{\text{Lab}} = 20$ and 30 eV and is the one adopted herein. Given the high collision energies ($E_{\text{Lab}} = 20$ and 30 eV), classical mechanics can describe satisfactorily the nuclear dynamics of the present system, and any possible inaccuracies by that description can be corrected with semiclassical techniques (see Section 4). In contrast, the electronic dynamics certainly requires a quantum description, but given the high number of electrons in $\text{H}^+ + \text{CF}_4$, a quantum treatment beyond a single-determinantal representation (like a multiconfiguration END [22]) would be impractical for a first exploration of this system.

The simplest END total wavefunction Ψ_{Total} is the product of nuclear Ψ_{N} and electronic Ψ_{e} parts: $\Psi_{\text{Total}} = \Psi_{\text{N}}\Psi_{\text{e}}$. The nuclear part Ψ_{N} is the product of $3N_{\text{N}}$ frozen, narrow-width, Gaussian wave packets:

$$\Psi_{\text{N}}(\mathbf{X}; \mathbf{R}, \mathbf{P}) = \prod_{i=1}^{3N_{\text{N}}} \exp \left\{ - \frac{(X_i - R_i)^2}{2\Delta R_i} + iP_i(X_i - R_i) \right\} \quad (1)$$

with average positions R_i , average momenta P_i , and position deviation (“width”) ΔR_i . The electronic part Ψ_{e} is a single-determinantal state $|\mathbf{z}; \mathbf{R}\rangle$ in the Thouless representation [20]:

$$\Psi_{\text{e}} = |\mathbf{z}; \mathbf{R}\rangle = \det[\chi_h(\mathbf{z}; \mathbf{R})] \quad (2)$$

where the dynamical spin-orbitals $\chi_h = \psi_h + \sum_{p=N_e}^K \psi_p z_{ph}$ ($1 \leq h \leq N_e$) are constructed in terms of a basis set of N_e occupied $\{\psi_h\}$ and $K - N_e$ virtual $\{\psi_p\}$ spin-orbitals with the complex parameters $\{z_{ph}\}$. Those basis spin-orbitals are constructed in terms of K atomic basis set functions centered on the traveling nuclear wave packets; for that reason, $|\mathbf{z}; \mathbf{R}\rangle$ depends upon the nuclear positions $\{R_i\}$. The spin-orbitals $\{\chi_h\}$ are taken as unrestricted with respect to spin in these simulations, but they are not orthogonal within spin blocks. Thouless representation of $|\mathbf{z}; \mathbf{R}\rangle$ provides a complex, continuous, nonredundant parameterization of the single-determinantal state in terms of a minimum number of parameters $\{z_{ph}\}$ that ensures a proper generalized phase space for the electronic dynamics [see Eq. (3)]. Those complex parameters $\{z_{ph}\}$ confer enough flexibility to $|\mathbf{z}; \mathbf{R}\rangle$ to describe various dynamical processes.

The END dynamics equations are obtained by applying the time-dependent variational principle [20, 23] to the trial wavefunction Ψ_{Total} with variational parameters $\{R_i(t), P_i(t), z_{ph}(t)$, and $z_{ph}^*(t)\}$. That is achieved by forming the quantum Lagrangian [23] of the system: $L(\Psi_{\text{Total}}, \Psi_{\text{Total}}^*) = \langle \Psi_{\text{Total}} | (i/2)(\partial/\partial t - \bar{\partial}/\partial t) - \hat{H} | \Psi_{\text{Total}} \rangle / \langle \Psi_{\text{Total}} | \Psi_{\text{Total}} \rangle$ and imposing stationarity to its associated quantum action S , $\delta S = \delta \int_{t_0}^{t_f} L(t) dt = 0$ [20, 23] in the narrow limit of the ΔR_i . In that way, the resulting END Euler–Lagrange equations for the variational parameters $\{R_i(t), P_i(t), z_{ph}(t)$, and $z_{ph}^*(t)\}$ are [20]:

$$\begin{bmatrix} i\mathbf{C} & 0 & i\mathbf{C}_R & 0 \\ 0 & -i\mathbf{C}^* & -i\mathbf{C}_R^* & 0 \\ i\mathbf{C}_R^T & -i\mathbf{C}_R^T & \mathbf{C}_{RR} & -\mathbf{I} \\ 0 & 0 & \mathbf{I} & 0 \end{bmatrix} \begin{bmatrix} \frac{d\mathbf{z}}{dt} \\ \frac{d\mathbf{z}^*}{dt} \\ \frac{d\mathbf{R}}{dt} \\ \frac{d\mathbf{P}}{dt} \end{bmatrix} = \begin{bmatrix} \frac{\partial E_{\text{Total}}}{\partial \mathbf{z}} \\ \frac{\partial E_{\text{Total}}}{\partial \mathbf{z}^*} \\ \frac{\partial E_{\text{Total}}}{\partial \mathbf{R}} \\ \frac{\partial E_{\text{Total}}}{\partial \mathbf{P}} \end{bmatrix} \quad (3)$$

where the total energy is $E_{\text{Total}} = \langle \Psi_{\text{Total}} | \hat{H} | \Psi_{\text{Total}} \rangle / \langle \Psi_{\text{Total}} | \Psi_{\text{Total}} \rangle = \sum_{i=1}^{3N_{\text{N}}} P_i^2 / 2M_i + \langle \mathbf{z}; \mathbf{R} | \hat{H}_{\text{e}} | \mathbf{z}; \mathbf{R} \rangle / \langle \mathbf{z}; \mathbf{R} | \mathbf{z}; \mathbf{R} \rangle$, the dynamical metric matrices are:

$$(\mathbf{C}_{XY})_{ij,kl} = -2\text{Im} \left| \frac{\partial^2 \ln S}{\partial X_{ik} \partial Y_{jl}} \right|_{\mathbf{R}'=\mathbf{R}} ;$$

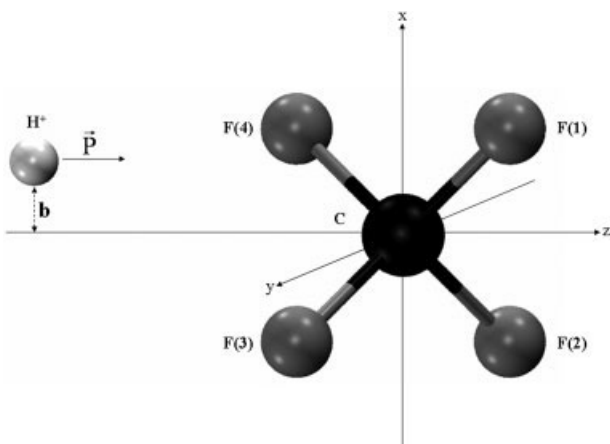


FIGURE 1. $\text{H}^+ + \text{CF}_4$ reactants initial conditions. The balls represent the six participating nuclei labeled: C, F(1), F(2), F(3), F(4), and H^+ . At initial time, CF_4 is at rest with its C atom on the coordinate center whereas H^+ with impact parameter b starts moving in parallel to the $+z$ -axis with momentum \vec{P} .

$$(\mathbf{C}_{X_{ik}})_{ph} = \left| \frac{\partial^2 \ln S}{\partial z_{ph}^* \partial X_{ik}} \right|_{R'=R};$$

$$\mathbf{C}_{ph,qg} = \left| \frac{\partial^2 \ln S}{\partial z_{ph}^* \partial z_{qg}} \right|_{R'=R} \quad (4)$$

and $S = \langle z'; \mathbf{R}' | z; \mathbf{R} \rangle$. Equation 3 expresses in symplectic notation [23, 24] the combined classical dynamics of the nuclei and the quantum dynamics of the electrons. In fact, the previous variational procedure and its resulting equations are a quantum generalization of the well-known Hamilton equations in symplectic notation from classical mechanics [23, 24]. In that way, the pairs of variables (R_i, P_i) and (z_{ph}, z_{ph}^*) are pairs of canonical variables in a generalized phase space [23, 24]. In a simulation, the reactants are prepared with initial nuclear positions and momenta $\{R_i^0\}$ and $\{P_i^0\}$ (see Fig. 1) and with initial electronic parameters $\{z_{ph}^0, z_{ph}^{0,*}\}$ that define the initial wavefunction Ψ_{Total}^i . A chemical reaction simulation is advanced by integrating Eq. (3) over time. At final time, the evolved wavefunction Ψ_{Total}^f contains all the necessary information to calculate relevant properties of the simulated reaction (e.g., transition probabilities, integral cross sections and DCSs, etc.).

3. Computational Details

All the present calculations have been conducted with the suite of programs *CSDYN* 1.0 (Morales

Group, *CSDYN*, Texas Tech University, Lubbock, TX, 2008–2009), developed from the *ENDyne* 2.7–2.8 codes (Deumens, *ENDyne: Electron Nuclear Dynamics Simulations*, Version 2, Release 8, Quantum Theory Project: University of Florida, Gainesville, FL, 1997). *CSDYN* passes all the run tests of *ENDyne* 2.7–2.8. Original features coded into *CSDYN* include a density-functional-theory/coherent-states dynamics method (not employed in this investigation), auxiliary programs to evaluate cross sections and other reaction properties (employed in this investigation), and several capabilities to make animations of the simulated reactions with the VMD program [25] (employed in this investigation). Some snapshots of those visualizations are shown in Figures 1 and 2.

The nuclear variables defining the initial conditions of the reactants H^+ and CF_4 in the present simulations are depicted in Figure 1. The nuclei initially representing the CF_4 molecule are labeled C, F(1), F(2), F(3), and F(4), respectively, whereas the nucleus initially in the incoming projectile H^+ is labeled H. In previous END simulations of $\text{H}^+ + \text{CH}_4$ [15], several initial orientations of the 10-electron CH_4 target were considered. However, because of the computational demands by the 42-electron CF_4 target, only one representative orientation will be considered in this preliminary study. Thanks to the almost spherical symmetry of CF_4 [8], the initial orientations of this target should not strongly affect the scattering results [8]. The selected orientation has the carbon atom C at the center of the coordinates (0.0, 0.0, 0.0) and the four fluorine atoms F(1), F(2), F(3), and F(4) at the points $(+a, +a, +a)$, $(-a, -a, +a)$, $(-a, +a, -a)$, $(+a, -a, -a)$, respectively, where $a = 1.443356$ a.u. To construct the electronic wavefunction, the 3–21G basis set [26] is placed on the six nuclei. The CF_4 molecule is initially at rest ($\mathbf{P}_C = \mathbf{P}_{F(1)} = \mathbf{P}_{F(2)} = \mathbf{P}_{F(3)} = \mathbf{P}_{F(4)} = 0$), and in its electronic ground state at the unrestricted Hartree–Fock self-consistent field [27] level. The H^+ projectile is initially placed at $(b, 0.0, -15.00$ a.u.) where b ($0 \leq b \leq +\infty$) is the impact parameter. The incoming projectile initially travels in parallel to the positive z -axis with momentum $\mathbf{P}_{\text{H}}^{\text{in}} = (0.0, 0.0, +P_{\text{H},z}^{\text{in}})$ corresponding to $E_{\text{Lab}} = (P_{\text{H},z}^{\text{in}})^2 / 2M_H = 20$ and 30 eV. At both energies, the impact parameter b is varied in the range of $0 \leq b \leq 9.9$ a.u. in steps of $\Delta b = 0.1$ a.u. From those initial conditions, the reaction simulations are run for a total time of 1300 a.u. That running time allows for a final products separation of at least 15.00 a.u. (i.e., the same separation as the reactants separations at initial time). After the simulations are

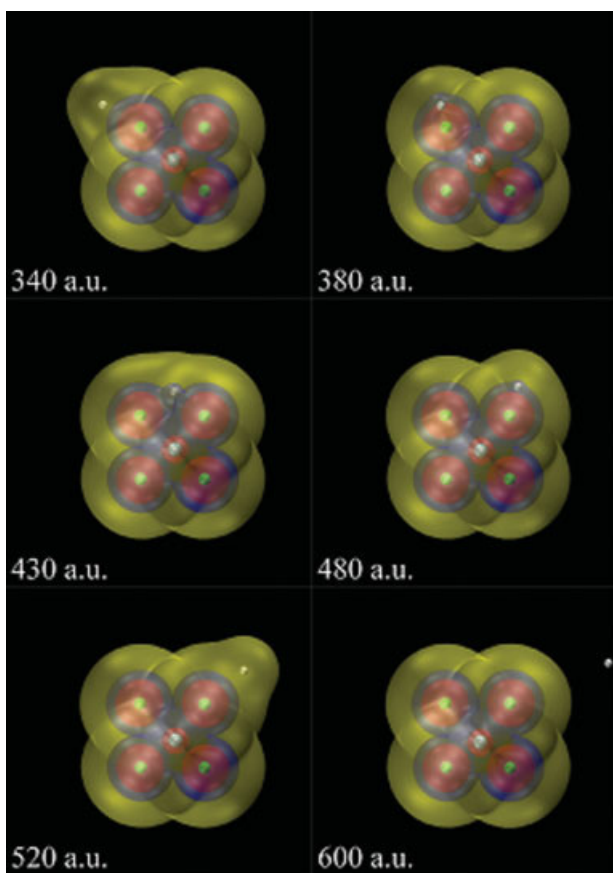


FIGURE 2. Six sequential snapshots of a simulation of $\text{H}^+ + \text{CF}_4$ at $E_{\text{Lab}} = 30$ eV from the impact parameter $b = 2.5$ a.u. Snapshot times are shown in a.u. Traveling nuclei are represented by small balls (green ball = F, gray ball = C, and white ball = H) along with some contour plots of the total electronic charge density (contour plots in gray, brown, and yellow colors). H^+ disturbs the CF_4 charge density during its flyby and transitorily acquires some electron density, but it finally leaves CF_4 without electrons. [Color figure can be viewed in the online issue, which is available at www.interscience.wiley.com.]

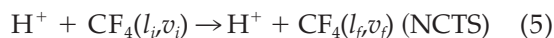
completed, the auxiliary programs in the CSDYN suite analyze the well-separated final products and calculate various reaction and scattering properties.

4. Results and Discussion

4.1 ANALYSIS OF TRAJECTORIES AND REACTIVE PROCESSES

The analysis of the simulated trajectories and of the final END waveFunction reveals that the

$\text{H}^+ + \text{CF}_4$ system at $E_{\text{Lab}} = 20$ and 30 eV is far less reactive than its $\text{H}^+ + \text{CH}_4$ counterpart at $E_{\text{Lab}} = 30$ eV [15]. The only process theoretically predicted in the present simulations is the noncharge-transfer scattering (NCTS):



where the incoming H^+ is deflected off after exciting the rotational and vibrational degrees of freedom of CF_4 . In all the simulations, the collision-induced vibrational and rotational excitations were moderate, especially in the case of the final rotational motion of CF_4 . An equivalent NCTS process was also predicted in the previous END study of $\text{H}^+ + \text{CH}_4$ at $E_{\text{Lab}} = 30$ eV [15] from many, but not all, the simulated trajectories. However, unlike the $\text{H}^+ + \text{CH}_4$ case, the $\text{H}^+ + \text{CF}_4$ simulations do not predict more reactive processes, such as charge-transfer scattering: $\text{H}^+ + \text{CF}_4(l_i v_i) \rightarrow \text{H}^0 + \text{CF}_4^+(l_f v_f)$, collision-induced dissociation: $\text{H}^+ + \text{CF}_4(l_i v_i) \rightarrow \text{H}^q + \text{F}^{q'} + \text{CF}_4^q(l_f v_f)$ ($q + q' + q'' = +1$), and hydrogen-fluorine rearrangement: $\text{H}^+ + \text{CF}_4(l_i v_i) \rightarrow \text{F}^q + \text{CHF}_3^{q'}(l_f v_f)$ ($q + q' = +1$). Reactive processes equivalent to the previous ones were predicted abundantly in the END study of $\text{H}^+ + \text{CH}_4$ [15]. The absence of charge-transfer processes in the present simulations can be clearly seen in the zero number of electrons (via Mulliken population analysis) on all the outgoing projectiles and in the animations of the evolving charge density (see discussion of Fig. 2 later). The $\text{H}^+ + \text{CF}_4$ experiment [8] could not measure any detectable charge-transfer process in agreement with the present simulations. The much lower reactivity of $\text{H}^+ + \text{CF}_4$ as compared with that of $\text{H}^+ + \text{CH}_4$ is easy to explain in terms of the chemical properties of fluorine. Fluorine is the second most electronegative element in the periodic table (after helium) and has a very low tendency to release electrons. Although the less electronegative carbon is more prone to donate electrons than fluorine, the carbon atom in CF_4 is so closely shielded by the electronegative fluorine atoms that it has a decreased capacity to interchange electrons. For those reasons, it is not surprising that no charge-transfer processes were predicted or measured in $\text{H}^+ + \text{CF}_4$. Finally, the high stability of the C—F bonds accounts for the lack of dissociation and rearrangement reactions in $\text{H}^+ + \text{CF}_4$.

An example of a simulated collision is given in Figure 2, where a series of six sequential snapshots of a $\text{H}^+ + \text{CF}_4$ collision at $E_{\text{Lab}} = 30$ eV from $b = 2.5$ a.u. is shown. In that figure, the traveling nuclei are represented by small balls (green balls = F, gray

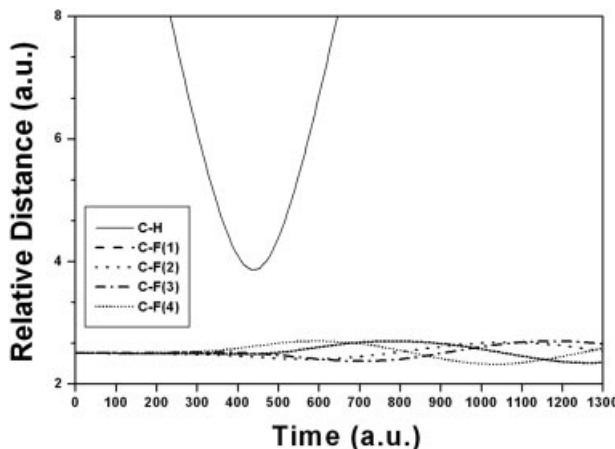


FIGURE 3. Selected nuclear relative distances versus time for $\text{H}^+ + \text{CF}_4$ at $E_{\text{Lab}} = 30$ eV from the impact parameter $b = 1.0$ a.u. The four C—F bonds get excited vibrationally by the time of the closest approach of H^+ (H) to the C on CF_4 (slightly after 400 a.u. of time).

ball = C, and white ball = H) along with several contour plots of the total electronic charge density corresponding to the evolving single-determinantal state $|\mathbf{z};\mathbf{R}\rangle$ (contour plots in gray, brown, and yellow colors). As revealed by those snapshots, the H^+ projectile disturbs the CF_4 charge density during its flyby and even transitorily acquires some charge density, but it finally leaves the CF_4 molecule without gaining electrons. In addition, an example of the vibrational excitations on CF_4 induced by the H^+ collision is shown in Figure 3. There, some relevant nuclear relative distances are plotted versus time for a simulated $\text{H}^+ + \text{CF}_4$ collision at $E_{\text{Lab}} = 30$ eV from $b = 1.0$ a.u. As seen in Figure 3, the four C—F bonds get vibrationally excited by the time of the shortest C—H separation (i.e., by the time of the closest H^+ approach to CF_4), just shortly after 400 a.u. of time. The vibrational excitations are noticeable at low impact parameters but become very slight at the high impact parameters that contribute to the measured scattering properties [8]. The END theory has an intimate connection with the coherent-state theory [13, 14, 28, 29]. vibrationally resolved properties of $\text{H}^+ + \text{CF}_4$ can be obtained by applying a coherent-states analysis [14] to its classical vibrational motions at final time. That procedure resulted in accurate vibrationally-resolved cross sections in the $\text{H}^+ + \text{H}_2$ system [14]. However, such an analysis is more involved with the tetrahedral CF_4 molecule and is postponed for a future investigation.

4.2 SCATTERING FEATURES

The classical scattering angle θ of the outgoing H^+ projectile with respect to its incoming z-direction is

$$\sin \theta = \frac{(P_{\text{Hx}}^{\text{out}})^2 + (P_{\text{Hy}}^{\text{out}})^2)^{1/2}}{(P_{\text{Hx}}^{\text{out}})^2 + (P_{\text{Hy}}^{\text{out}})^2 + (P_{\text{Hz}}^{\text{out}})^2}^{1/2}; \quad (0 \leq \theta \leq 180^\circ) \quad (6)$$

where $\{P_{\text{Hi}}^{\text{out}}\}$ ($i = x, y, z$) are the outgoing projectile momentum components at final time. Classical scattering angle functions $\theta(b)$ versus the projectile impact parameters b at collision energies $E_{\text{Lab}} = 20$ and 30 eV are depicted in Figure 4; in addition, relevant quantities associated with $\theta(b)$ are listed in Table I. At both energies, the predicted scattering angle functions $\theta(b)$ reproduce well-known scattering features that are expected for the present system [30]. For instance, both $\theta(b)$ display primary rainbow angles $\theta_R^{\text{CL}} = \theta(b_R^l)$ as maxima at relatively high impact parameters $b_R^l([d\theta(b)/db]_{b=b_R^l} = 0^\circ)$ (see Table I) and zero scattering angles $\theta_G(b_G) = 0^\circ$ at impact parameters $b_G < b_R^l$ ($b_G = 3.0$ and 2.9 a.u. at 20 and 30 eV, respectively). Those zero angles are known as (forward) glory scattering angles [30] and correspond to an outgoing projectile that has not been deflected from its original traveling direction. At even lower impact parameters, $b < b_G$, both scattering angle functions $\theta(b)$ become sharply increasing. The observed features in both $\theta(b)$ are easily explained in terms of the projectile-target interactions [30]. For instance, when $b > b_G$, the projectile mostly experiences the long-range attraction by the target and ends up deflected toward the z-axis. On the other hand,

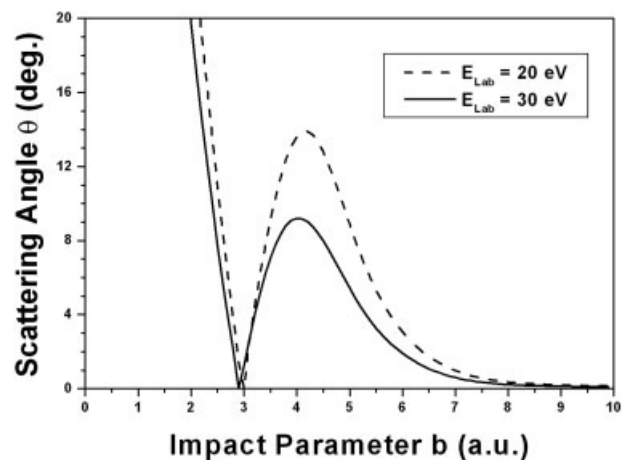


FIGURE 4. Scattering angle function $\theta(b)$ versus impact parameter b for $\text{H}^+ + \text{CF}_4$ at $E_{\text{Lab}} = 20$ and 30 eV.

TABLE I

Primary rainbow angles per collisional energy: Calculated and experimental [8] results.

Energy (eV)	Primary rainbow angles			
	Impact parameter, b_R^l (a.u.)	Rainbow angle (classical) $\theta_R^{l\text{CL}}(^{\circ})$	Rainbow angle (semiclassical) $\theta_R^{l\text{SC}}(^{\circ})$	Rainbow angle (experimental) $\theta_R^{l\text{Exp.}}(^{\circ})$
20	4.2	13.9	12.7	14.0
30	4.0	9.2	7.6	9.5

when $b < b_G$, the projectile mostly experiences the short-range repulsion by the target and ends up deflected from the z -axis. At exactly $b = b_G$, the transition from repulsive to attractive scattering takes place and manifests as a glory scattering $\theta_G(b_G) = 0^{\circ}$ indicating no deflection. Within the long-range attractive interval $(b_G, +\infty)$, the attraction is the weakest at the highest impact parameters (i.e., at long projectile-target separations) but increases at lower impact parameters (i.e., at shorter projectile-target separations) and reaches a maximum in strength at b_R^l . In that way, the primary rainbow angle $\theta_R^{l\text{CL}}$ corresponds to a maximum attractive deflection. As soon as $b < b_R^l$, the overall attractive scattering decreases, eventually becomes zero at exactly $b = b_G$, and finally reverts into a repulsive scattering when $b < b_G$.

As seen in Table I, the calculated classical primary rainbow angles $\theta_R^{l\text{CL}}$ agree well with their experimental counterparts $\theta_R^{l\text{Exp.}}$ [8] at the two considered energies. The experiment also detected two faint secondary rainbow angles $\theta_R^{l\text{Exp.}} = 8.5^{\circ}$ and 5° at $E_{\text{Lab}} = 20$ and 30 eV, respectively [8]. Those secondary angles are not predicted by the present simulations that include only one initial target orientation. However, previous studies [3, 14] showed that not all the initial target orientations render scattering angle functions with secondary rainbow angles; furthermore, in those studies, the appearance of a secondary rainbow angle always excluded that of a glory angle and vice versa. The appearance of a glory angle along with the absence of a secondary rainbow angle in the present simulations is in agreement with the last finding. Only the consideration of additional initial target orientations in the simulations may lead to the prediction of secondary rainbows.

4.3. TOTAL DCS

The main experimental results for the $H^+ + CF_4$ system at collision energies $E_{\text{Lab}} = 20$ and 30 eV are the total NCTS DCS $[d\sigma(\theta)/d\Omega]_{i \rightarrow f}$ [8]. Since

classical mechanics is being prescribed for the nuclei, a first estimate to the experimental NCTS DCS is the classical NCTS DCS [24, 30]:

$$\left[\frac{d\sigma(\theta)}{d\Omega} \right]_{i \rightarrow f}^{\text{CL}} = \sum_{m=1}^N \left[\frac{d\sigma(\theta)}{d\Omega} \right]_m = \sum_{m=1}^N \frac{b_m}{\sin \theta |d\theta(b)/db|_{b=b_m}} \quad (7)$$

where m labels the N classical trajectories that starting from the impact parameters b_m end up in the scattering direction θ . For the scattering angle functions $\theta(b)$ in Figure 4, $N = 3$ if $\theta < \theta_R^{l\text{CL}}$ (i.e., one repulsive and two attractive trajectories contribute to the DCS; lit region) and $N = 1$ if $\theta > \theta_R^{l\text{CL}}$ (i.e., only one repulsive trajectory contributes to the DCS; shadow region). A classical DCS provides an acceptable estimate to the experimental DCS at scattering angles θ not close to a rainbow angle $\theta_R^{l\text{CL}}$. However, the classical DCS in Eq. (7) produces an unphysical rainbow singularity at $\theta = \theta_R^{l\text{CL}}$ through $|d\theta(b)/db|_{b=b_m} = 0$ in that scattering direction [24, 30]. A more accurate and singularity-free estimate to the experimental DCS is provided by the semiclassical DCS expression. The latter is obtained by evaluating the quantum DCS expression in the limit of $\hbar \rightarrow 0$. The specific semiclassical approximation for a given scattering problem depends upon the topology of its associated classical scattering angle function $\theta(b)$. For the present $\theta(b)$ having only one rainbow angle, the uniform Airy approximation [30, 31] provides the most accurate semiclassical DCS:

$$\left[\frac{d\sigma(\theta)}{d\Omega} \right]_{i \rightarrow f}^{\text{SC}} = |f_1(\theta) + f_{23}^{\text{U.Airy}}(\theta)|^2 \quad (8)$$

where $f_1(\theta)$ and $f_{23}^{\text{U.Airy}}(\theta)$ are the scattering amplitudes corresponding to the one repulsive (1) and the two attractive (2 and 3) trajectories, respectively,

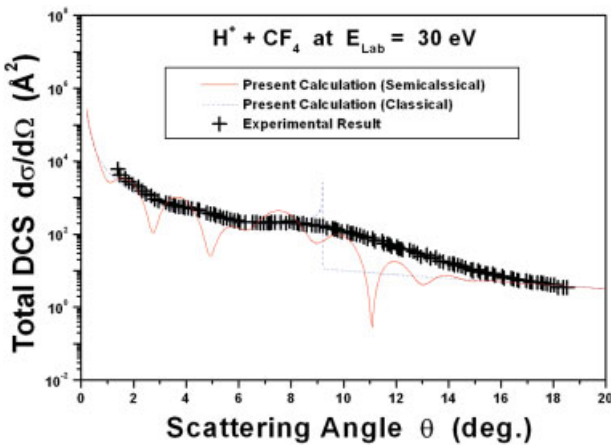


FIGURE 5. Total NCTS differential cross sections (DCS; $d\sigma(\theta)/d\Omega$) versus scattering angle (θ) for $H^+ + CF_4$ at $E_{Lab} = 30$ eV: semiclassical, classical, and experimental results. [Color figure can be viewed in the online issue, which is available at www.interscience.wiley.com.]

$$f_1(\theta) = \left| \frac{d\sigma(\theta)}{d\Omega} \right|_1^{1/2} \exp(iA_1);$$

$$\begin{aligned} f_{23}^{U, \text{Airy}}(\theta) = & \pi^{1/2} \exp \left[i \left(A_{23} - \frac{1}{4}\pi \right) \right] \left\{ \left[\left| \frac{d\sigma(\theta)}{d\Omega} \right|_2^{1/2} \right. \right. \\ & + \left| \frac{d\sigma(\theta)}{d\Omega} \right|_3^{1/2} \left. \xi_{23}^{1/4} Ai(-\xi_{23}) - i \left[\left| \frac{d\sigma(\theta)}{d\Omega} \right|_2^{1/2} \right. \right. \\ & \left. \left. - \left| \frac{d\sigma(\theta)}{d\Omega} \right|_3^{1/2} \xi_{23}^{-1/4} Ai'(-\xi_{23}) \right\} \quad (9) \end{aligned}$$

where $Ai(\xi_{-23})$ and $Ai'(\xi_{-23})$ are the Airy function and its first derivative, respectively. In Eq. (9), the classical DCS per trajectory $[d\sigma(\theta)/d\Omega]_m$ [Eq. (7)], the phases $A_1(\theta)$ and $A_{23}(\theta)$ [31], and the argument $\xi_{23}(\theta)$ [31] can all be evaluated from classical trajectories data. Near the rainbow angle $\theta_R^{I, CL}$, the uniform Airy scattering amplitude $f_{23}^{U, \text{Airy}}(\theta)$ reduces to the simpler transitional Airy approximation amplitude $f_{23}^{T, \text{Airy}}(\theta)$ [31]. The uniform Airy approximation has been used several times in the context of the END theory and provided very accurate DCSs for $H^+ + H_2$ [14], $H^+ + CH_4$ [15], and $H^+ + H_2O$ [18] *inter alia*. Unlike the classical DCS in Eq. (7), the semiclassical DCS in Eq. (8) does not display an unphysical rainbow singularity at the classical rainbow $\theta_R^{I, CL}$ but a bounded rainbow maximum at a

semiclassical rainbow angle $\theta_R^{I, SC} < \theta_R^{I, CL}$. The calculated values of $\theta_R^{I, SC}$ are listed in Table I.

The performance of the classical and semiclassical DCS from the present END simulations is examined in Figures 5 and 6. There, the calculated total NCTS DCS for $H^+ + CF_4$ at $E_{Lab} = 30$ eV (see Fig. 5) and at $E_{Lab} = 20$ eV (see Fig. 6), at the classical [Eq. (7)] and the semiclassical [Eqs. (8) and (9)] levels, are plotted versus the scattering angle θ along with their corresponding experimental results [8]. The last ones were reported un-normalized, but to make comparisons, they have been normalized in Figures 5 and 6. Each experimental DCS was individually normalized to match both its classical and semiclassical counterparts as close as possible. Such normalization procedures are usual in these types of studies [3, 14, 15, 18]. In Figures 5 and 6, each experimental DCS was normalized individually to facilitate its visual comparison with the calculated DCS; a more rigorous comparison employing the same normalization constant for both DCS is shown in Figure 7 (see discussion later). In Figures 5 and 6, the classical DCS agree fairly with the experimental ones but show unphysical rainbow angle singularities at $\theta = \theta_R^{I, CL}$ (see Table I). Contrastingly, the semiclassical DCS agree better with the experimental ones and do not display singularities. The semiclassical DCS show an oscillatory pattern produced by the semiclassical phases in Eqs. (8) and (9). That genuine effect is always perceptible in a semiclassical DCS corre-

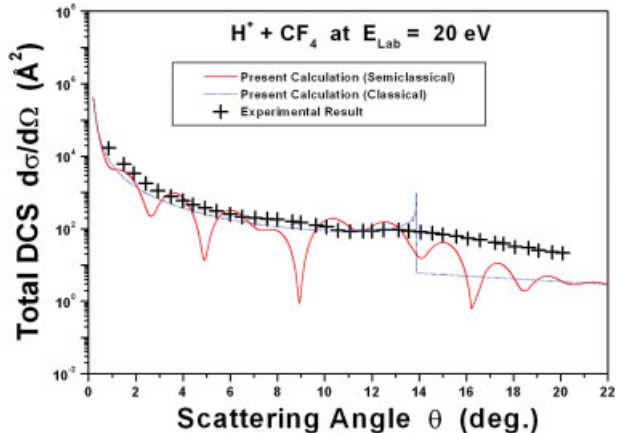


FIGURE 6. Total NCTS differential cross sections (DCS; $d\sigma(\theta)/d\Omega$) versus scattering angle (θ) for $H^+ + CF_4$ at $E_{Lab} = 20$ eV: semiclassical, classical, and experimental results. [Color figure can be viewed in the online issue, which is available at www.interscience.wiley.com.]

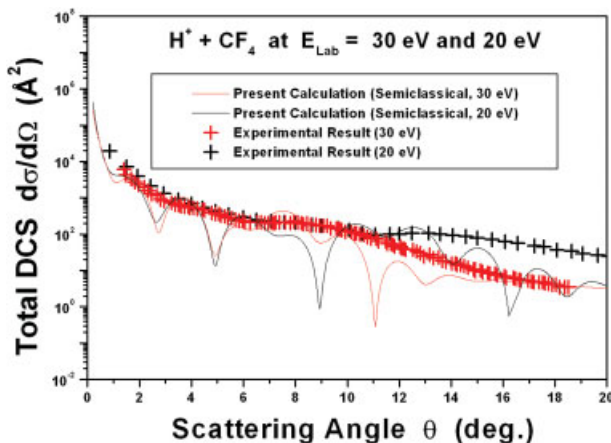


FIGURE 7. Total NCTS differential cross sections (DCS; $d\sigma/d\Omega$) versus scattering angle (θ) for $H^+ + CF_4$ at $E_{Lab} = 30$ and 20 eV: semiclassical and experimental results. [Color figure can be viewed in the online issue, which is available at www.interscience.wiley.com.]

sponding to an individual target orientation [14, 15, 18]. However, as proven in previous studies [14, 15, 18], if several target orientations are considered and their respective semiclassical DCS are averaged, the resulting DCS will show a mitigated oscillatory pattern as that shown by the experimental result. The latter has a mitigated oscillatory pattern because it too averages several DCS contributions from different target orientations in the experimental apparatus. The classical DCS do not show that oscillatory pattern in an artificial way since they lack the semiclassical phases in their expression [Eq. (7)]. The semiclassical total NCTS DCS for $H^+ + CF_4$ at $E_{Lab} = 30$ eV is in good agreement with its experimental counterpart at all the measured scattering angles. On the other hand, the semiclassical total NCTS DCS for $H^+ + CF_4$ at $E_{Lab} = 20$ eV is in good agreement with its experimental counterpart at scattering angles $\theta < \theta_R^{l,CL}$ (lit region) but in a less satisfactory agreement at scattering angles $\theta > \theta_R^{l,CL}$ (shadow region). The main contribution to a semiclassical DCS in the shadow region comes from the Airy function term in the semiclassical expression. Since semiclassical approximations work well at high energies, the semiclassical DCS in the shadow region at $E_{Lab} = 20$ eV might perform less accurately than that at $E_{Lab} = 30$ eV. However, it will be necessary to include additional target orientation in the simulations, to obtain more complete DCS, to finally con-

firm the good result at $E_{Lab} = 30$ eV and to improve that at $E_{Lab} = 20$ eV.

For a final comparison, the semiclassical and the experimental NCTS DCS for $H^+ + CF_4$ at $E_{Lab} = 30$ eV and $E_{Lab} = 20$ eV are plotted together versus the scattering angle θ in Figure 7. In that figure, the experimental DCS at $E_{Lab} = 30$ eV is normalized in the same way as that used in Figure 5; however, the experimental DCS at $E_{Lab} = 20$ eV is now normalized with the same normalization constant used for its counterpart at $E_{Lab} = 30$ eV. The normalization constant at $E_{Lab} = 30$ eV is given preference because at that energy the calculated DCS are in a better overall agreement with the experimental result (Figs. 5 and 6). The normalized experimental DCS at $E_{Lab} = 20$ eV in Figure 7 is slightly changed from its location in Figure 6, falling within the same orders of magnitude per point, and keeping its comparison with its calculated counterparts essentially the same. This more astringent normalization procedure renders proportionate values of both experimental DCS that can be compared precisely and at once with the absolute values of the calculated DCS. At any rate, Figure 7 corroborates the conclusions made about the calculated DCS in Figures 5 and 6.

5. Concluding Remarks

The $H^+ + CF_4$ reaction at collision energies $E_{Lab} = 20$ and 30 eV has been investigated with the END theory. The level of END herein employed prescribes a classical-mechanics description for the nuclei and a single-determinantal representation for the electrons. Since the number of electrons in $H^+ + CF_4$ is considerable for time-dependent, direct-dynamics simulations, only one representative target orientation was considered for the initial conditions of the present calculations (see Fig. 1). The results include visualizations of the simulated collisions, analysis of the final products, and calculations of various scattering properties. Present simulations always predict noncharge-transfer scattering (NCTS) for $H^+ + CF_4$ and rule out other types of processes such as charge-transfer, collision-induced dissociation, and rearrangement reactions. The low reactivity of $H^+ + CF_4$ as compared with that of the previously studied $H^+ + CH_4$ is explicable in terms of the high electronegativity of the fluorine atom and of the strength of the C—F bonds. The calculated semiclassical total NCTS DCS for $H^+ + CF_4$ at $E_{Lab} = 30$ eV is in good agree-

ment with its experimental counterpart at all the measured scattering angles. The calculated semi-classical total NCTS DCS for $H^+ + CF_4$ at $E_{Lab} = 20$ eV is in good agreement with its experimental counterpart at scattering angles lower than the rainbow angle but is in a less satisfactory agreement at higher scattering angles. The results of this preliminary investigation are promising and give an impetus for a more exhaustive study of this system in the future.

ACKNOWLEDGMENTS

It is with immense pleasure that three of us (R.S., S.A.P., and J.A.M.) contribute to this special issue honoring Frank Harris on the occasion of his 80th birthday. Frank's accomplishments as a scientist and as a mentor are well recognized in the community, but we admire Frank for something other than those: his acceptance of us as equals, not as juniors, during our exhilarating times in the old QTP. We thank him for all his wise guidance, wish him well on his 80th birthday, and hope that there will be many more! All the present calculations have been conducted at the Texas Tech University High Performance Computer Center (TTU HPCC), to which generous use of computer time and technical support are gratefully acknowledged.

References

1. Udseth, H.; Giese, F. C.; Gentry, R. W. *J Chem Phys* 1974, 60, 3051.
2. Krutein, J.; Linder, F. *J Chem Phys* 1979, 71, 599.
3. Niedner, G.; Noll, M.; Toennies, P. J.; Schlier, C. *J Chem Phys* 1987, 87, 2685.
4. Noll, M.; Toennies, P. J. *J Chem Phys* 1986, 85, 3313.
5. Friedrich, B.; Gianturco, A. F.; Niedner, G.; Noll, M.; Toennies, P. J. *J Phys B* 1987, 20, 3725.
6. Friedrich, B.; Niedner, G.; Noll, M.; Toennies, P. J. *J Chem Phys* 1987, 87, 5256.
7. Niedner, G.; Noll, M.; Toennies, P. J. *J Chem Phys* 1987, 87, 2067.
8. Chiu, N. Y.; Friedrich, B.; Maring, W.; Niedner, G.; Noll, M.; Toennies, P. J. *J Chem Phys* 1988, 88, 6814.
9. Aristov, N.; Niednerschatteburg, G.; Toennies, P. J.; Chiu, N. Y. *J Chem Phys* 1991, 95, 7969.
10. Gierz, U.; Noll, M.; Toennies, P. J. *J Chem Phys* 1985, 83, 2259.
11. Tully, C. J.; Preston, R. K. *J Chem Phys* 1971, 55, 562.
12. Baer, M.; Niednerschatteburg, G.; Toennies, P. J. *J Chem Phys* 1989, 91, 4169.
13. Deumens, E.; Diz, A.; Longo, L. R.; Öhrn, Y. *Rev Mod Phys* 1994, 66, 917.
14. Morales, J. A.; Diz, A.; Deumens, E.; Öhrn, Y. *J Chem Phys* 1995, 103, 9968.
15. Jacquemin, D.; Morales, J. A.; Deumens, E.; Öhrn, Y. *J Chem Phys* 1997, 107, 6146.
16. Malinovskaya, A. S.; Cabrera-Trujillo, R.; Sabin, R. J.; Deumens, E.; Öhrn, Y. *J Chem Phys* 2002, 117, 1103.
17. Morales, J. A.; Maiti, B.; Yan, Y.; Tsereteli, K.; Laraque, J.; Addepalli, S.; Myers, C. *Chem Phys Lett* 2005, 414, 405.
18. Hedström, M.; Morales, J. A.; Deumens, E.; Öhrn, Y. *Chem Phys Lett* 1997, 279, 241.
19. Quinet, O.; Deumens, E.; Öhrn, Y. *Int J Quantum Chem* 2008, 109, 259.
20. Deumens, E.; Diz, A.; Longo, L. R.; Öhrn, Y. *Rev Mod Phys* 1994, 66, 917.
21. Deumens, E.; Öhrn, Y. *J Phys Chem A* 2001, 105, 2660.
22. Deumens, E.; Öhrn, Y.; Weiner, B. *J Math Phys* 1991, 32, 1166.
23. Kramer, P.; Saraceno, M. *Geometry of the Time-Dependent Variational Principle in Quantum Mechanics*; Springer-Verlag: New York, 1981.
24. Goldstein, H.; *Classical Mechanics*; Addison-Wesley: Reading, MA, 1980.
25. Humphrey, W.; Dalke, A.; Schulten, K.; *Molec. J. Graphics* 1996, 14, 33.
26. Binkley, S. J.; Pople, A. J.; Hehre, J. W. *J Am Chem Soc* 1980, 102, 939.
27. McWeeney, R. *Methods of Molecular Quantum Mechanics*; Academic Press: London, 1992.
28. Klauder, R. J.; Skagerstam, S. B. *Coherent States, Application in Physics and Mathematical Physics*; World Scientific, Singapore, 1985.
29. Morales, J. A.; Deumens, E.; Öhrn, Y. *J Math Phys* 1999, 40, 766.
30. Child, S. M. *Molecular Collision Theory*; Dover Publications, Inc.: Mineola, NY, 1984.
31. Connor, J. N. L.; Farrelly, D. *J Chem Phys* 1981, 75, 2831.